OPEN ACCESS
IOP Publishing | International Atomic Energy Agency
Nuclear Fusion
Nucl. Fusion **65** (2025) 066022 (16pp)
https://doi.org/10.1088/1741-4326/add6b4

Anisotropic distribution of alpha particles in a tokamak reactor

Youjun Hu[1,*], Xingyuan Xu[1], Yingfeng Xu[2], Yifeng Zheng[1], Guoqiang Li[1], Zhiyong Qiu[1] and Youwen Sun[1]

[1] Institute of Plasma Physics, Chinese Academy of Sciences, Hefei 230031, China
[2] College of Science, Donghua University, Shanghai 201620, China

E-mail: yjhu@ipp.cas.cn

Received 8 December 2024, revised 9 April 2025
Accepted for publication 9 May 2025
Published 19 May 2025

Abstract

We carried out systematic study of neoclassical equilibrium distribution of α particles born from deuterium–tritium nuclear fusion in a tokamak reactor. The distribution in the phase space is visualized in various 2D planes. We studied a previously known but less investigated phenomenon—the co-current flow of α particles. We gave detailed explanation for this flow by examining the collisionless evolution of toroidal filament sources, using both the guiding-center drift model and full orbit model. We found that the flow appears because of the co-count asymmetry, which makes co-going α particles on average stay in weaker magnetic field region than that of the counter-going ones.

Keywords: deuterium–tritium fusion, energetic alpha particles, neoclassical transport, ripple field, Monte-Carlo simulation, anisotropic distribution

(Some figures may appear in colour only in the online journal)

1. Introduction

Alpha particles born from deuterium–tritium fusion in tokamak reactors are initially isotropic in the velocity space (assuming that the reactants are isotropic, which is usually a good approximation). Is the steady-state alpha particle distribution also isotropic? The answer is no, for several reasons. Even in the collisionless limit, there are two mechanisms that can generate anisotropy. The first one is the well known difference between the parallel and perpendicular dynamics (defined with respect to the equilibrium magnetic field). The second one is the less known asymmetry in the parallel dynamics: the orbit difference between particles initially moving along the plasma current (co-going) and those initially moving opposite to the plasma current (counter-going). The co-going particles on average reside in a weaker magnetic field region than that of counter-going particles, resulting the asymmetry. We refer to this as the co-counter asymmetry. As a result of this asymmetry, a net co-current toroidal flow of α particles is generated. (Details are discussed in section 4.)

Research on anomalous transport of energetic α particles need an initial neoclassical equilibrium distribution of α particles as input. This input can be obtained either by analytical theories or by numerical simulations. Analytical theories rely on simplification (e.g. zero drift-orbit width, no pitch angle scattering, no energy diffusion, no edge loss, no ripple field, etc). Simulations can drop these simplifications and give more realistic particle distributions. In this paper, we present steady-state α particle distribution obtained from neoclassical simulations in a tokamak reactor, China Fusion Engineering Testing Reactor (CFETR) [1]. The distribution in the phase

* Author to whom any correspondence should be addressed.

space is visualized in various 2D planes. Simulations were performed by using the TGCO [2], which is a Monte-Carlo test particle code similar to NUBEAM [3], OFMC [4], ASCOT [5], ORBIT [6], SPIRAL [7], and many others [8–11].

Some authors use artificially large collisional frictions in simulations of α particles collisional process to accelerate the slowing-down, in order to reduce computational cost [12]. Although, this trick may be safe for some situations in drawing valid physical conclusions from the simulations, it is still interesting to do simulations using the realistic slowing-down rate and see what happens. This work adopts this brute-force method.

This paper is organized as follows. Section 2 provides the simulation setup (equilibrium field and α particle source) and a brief description of the physical model. Section 3 presents the steady-state α particle distribution in the phase space, where anisotropy was observed. Section 4. discuss the reason for the anisotropy. Section 5 takes into account of the 3D ripple field and examines its effect on the α particle distribution. Summary and discussions are given in section 6.

2. Simulation setup

2.1. Equilibrium magnetic field

The 2D equilibrium magnetic field is given by

$$\mathbf{B} = \nabla\Psi \times \nabla\phi + g\nabla\phi, \tag{1}$$

i.e.

$$B_R = -\frac{1}{R}\frac{\partial\Psi}{\partial Z}, \tag{2}$$

$$B_Z = \frac{1}{R}\frac{\partial\Psi}{\partial R}, \tag{3}$$

$$B_\phi = \frac{g}{R}, \tag{4}$$

where (R,ϕ,Z) are the right-handed cylindrical coordinates, R is the distance from the machine symmetric axis, ϕ is the toroidal angle, Z is the vertical height, B_R, B_Z, and B_ϕ are the components of $\mathbf{B}$, $\Psi(R,Z)$ is the poloidal flux function (poloidal magnetic flux per radian), $g = B_\phi R = g(\Psi_N)$ is the toroidal field function, where $\Psi_N = (\Psi - \Psi_0)/(\Psi_b - \Psi_0)$ is the normalized poloidal flux, Ψ_0 and Ψ_b are Ψ's values at the magnetic axis and LCFS (last closed flux surface), respectively. Both $\Psi(R,Z)$ and $g(\Psi_N)$ are given numerically by EFIT output file (gfile) [13]. In terms of Ψ, the plasma toroidal current density is given by

$$J_\phi = -\frac{1}{\mu_0 R}\frac{\partial^2\Psi}{\partial Z^2} - \frac{1}{\mu_0}\frac{\partial}{\partial R}\left(\frac{1}{R}\frac{\partial\Psi}{\partial R}\right), \tag{5}$$

where μ_0 is vacuum magnetic permeability. If one wants to reverse the direction of J_ϕ, then use the transform $\Psi \to (-\Psi)$. This also reverses the direction of the poloidal magnetic field. We use this transform when verifying that α particle toroidal flow is always along the plasma current direction.

Later in this paper, we take into account the ripple field, which is considered as 3D perturbation superposed on the 2D equilibrium field.

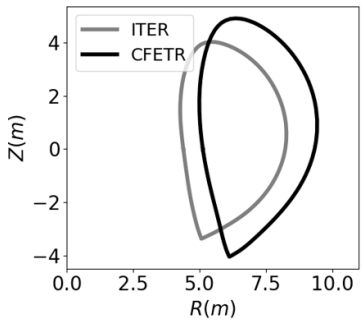

Figure 1. Comparison of LCFS between CFETR and ITER tokamak.

We use CFETR [1] as an example to investigate properties of the alpha particle distribution in a tokamak reactor. Figure 1 compares the size of CFETR with that of ITER.

CFETR has gone through several design iterations by integrated modeling [1]. One of the envisioned operation scenario is the so-called hybrid scenario, which has a flat safety factor profile near the core with on-axis safety factor value about 1, as is shown in figure 2(*b*). We did simulations in this scenario.

Figure 2(*a*) plots the first wall and some representative magnetic surfaces. The directions of the toroidal plasma current and magnetic field are opposite to each other, with the $B_\phi < 0$ and $I_\phi > 0$, as is indicated on the figure. Figure 2(*c*) plots the radial profiles of ion temperature, ion number density, electron temperature, and electron number density. Main ion species are deuterium and tritium, which are assumed to be of equal number density and of equal temperature. Impurities are Helium (energetic α particles + Helium ash) and Argon, with concentration that makes the ion effective charge number $Z_{\rm eff} = 2.0$. Figure 2(*d*) plots the radial profiles of the total pressure $P_{\rm total}$, bulk plasma pressure $P_{\rm main}$, and energetic α particle pressure P_α. Here $P_{\rm main} = n_{\rm e}T_{\rm e} + 2n_{\rm D}T_{\rm i}$, where $n_{\rm D} = n_{\rm T}$ is the deuterium/tritium number density. The total pressure $P_{\rm total} \approx P_{\rm main} + P_\alpha$, which is the pressure used in the EFIT equilibrium reconstruction. Helium ash and Argon impurities' contribution to the pressure is negligible. The α particle pressure P_α is computed using approximate analytical theory (the formulas are provided in appendix B). Later in the paper, we compare this pressure with that obtained in simulations, which shows they roughly agree with each other, indicating self-consistency of the equilibrium reconstruction and our simulations.

Total fusion power is 0.97GW in this scenario, with 0.19GW carried by α particles and the remainder carried by neutrons.

2.2. α particle source

We sample α particle birth positions in (R,ϕ,Z) coordinates, using the Monte-Carlo rejection method. The sampling probability function is proportional to $RF_{\rm rate}(\Psi_N(R,Z))$, where $F_{\rm rate}$ is the fusion rate (i.e. number of fusion reactions in unit volume and unit time; the details are given in appendix A). The resulting marker density is proportional to the fusion rate, and only depends on Ψ_N in the magnetic coordinate system. The marker weight is equal among all markers.

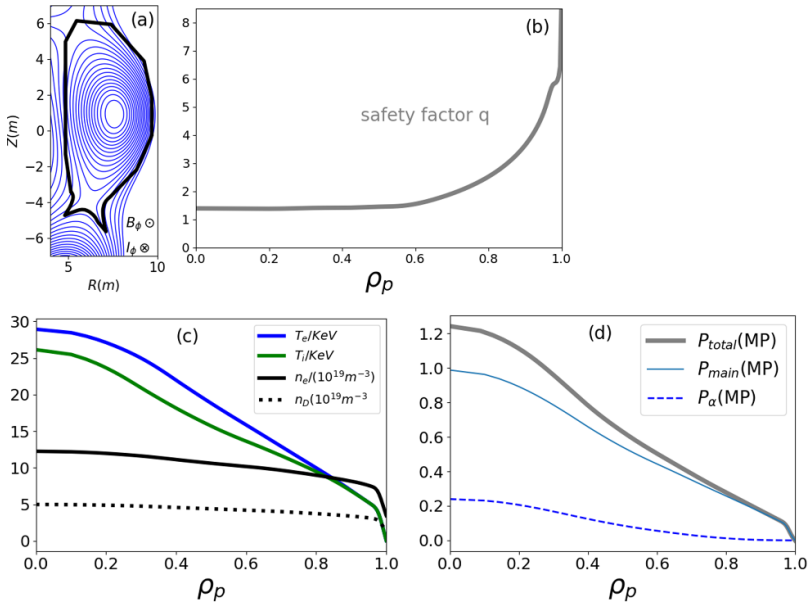

Figure 2. (*a*) Magnetic surfaces and the first wall (bold black line). (*b*) Radial profile of safety factor. (*c*) Radial profiles of ion temperature, ion number density, electron temperature, electron number density. (*d*) Radial profiles of total pressure P_{total}, bulk plasma pressure P_{main}, and energetic α particle pressure P_α. The radial coordinate ρ_p is defined by $\rho_p = \sqrt{\Psi_N}$. The directions of toroidal field and plasma current are indicated in (*a*). The magnetic axis is at $(R = 7.6\,\text{m}, Z = 0.93\,\text{m})$, and $B_{\phi,\text{axis}} = -6.11\,\text{T}$. Total plasma current $J_\phi = 13\,\text{MA}$. The safety factor value at $\Psi_N = 0.95$: $q95 = 5.75$.

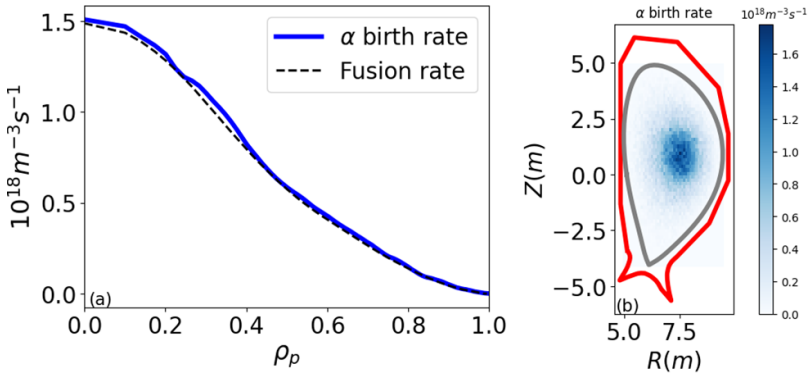

Figure 3. (*a*) Radial profile of fusion rate and α particle birth rate. Here α particle birth rate is obtained from Monte–Carlo samplings of the fusion rate. (*b*) Distribution of α particle birth rate in the poloidal plane.

To verify the accuracy of the Monte–Carlo sampling, figure 3(*a*) plots the numerical radial distribution of α particle birth rate, which shows agreement with the fusion rate profile. Figure 3(*b*) plots the two-dimensional (2D) distribution of α particle birth rate in the poloidal plane.

Particle velocities are sampled according to the isotropic distribution of single energy $(E = 3.5\,\text{MeV})$. Figure 4(*a*) plots the numerical birth distribution over the pitch $(p \equiv v_\parallel/v)$, which shows nearly uniform distribution, consistent with the isotropic marker loading. Figures 4(*b*) and (*c*) separate the total particle distribution into trapped one and passing one. Although they are no longer uniform, they are still symmetric about $p = 0$, indicating they do not carry any net current.

One may emphasize the difference between the parallel velocity $v_\parallel$ and the toroidal velocity v_ϕ. To check whether this difference is significant, figures 4(*d*)–(*f*) plot the distribution over v_ϕ/v, which shows similar behavior as that of $v_\parallel/v$, indicating the difference is insignificant. Here v_ϕ is the gyro-averaged toroidal velocity, $v_\phi = (v_\parallel \mathbf{b} + \mathbf{v}_\text{d}) \cdot \hat{\boldsymbol{\phi}}$, where $\mathbf{v}_\text{d}$ is the magnetic drift velocity (gradient + curvature drift).

Figure 5 plots the initial positions of α particle markers in (P_ϕ, Λ) plane, where $P_\phi \equiv m_\alpha v_\parallel g/B + Z_\alpha e\Psi$ is the canonical toroidal angular momentum, m_α and $Z_\alpha e$ are the mass and charge of α particle, respectively, $\Lambda = \mu B_{\text{axis}}/E$ is the normalized magnetic moment, and μ is the magnetic moment defined by $\mu = mv_\perp^2/(2B)$ with $v_\perp$ being the perpendicular speed. Both P_ϕ and Λ are constants of motion in the equilibrium field. Using the passing-trapped boundary shown in the figure, we found that 28% of α particles are born in the trapped region.

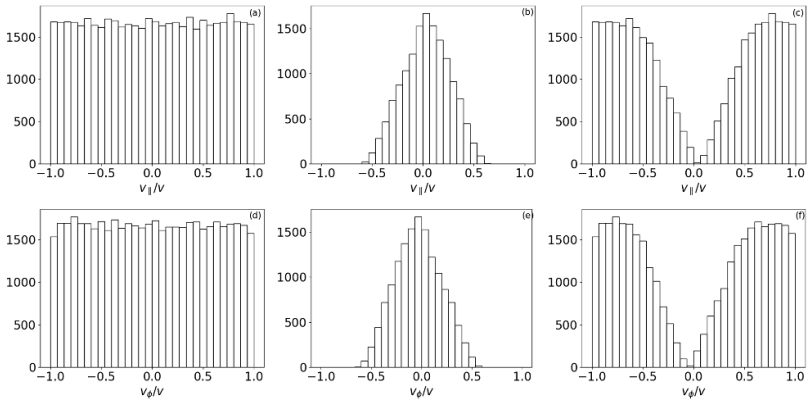

Figure 4. Histogram of 5×10^4 Monte–Carlo samplings of α particle birth distribution about $v_\parallel/v$ and v_ϕ/v. Left: all (trapped+passing), Middle: only trapped, Right: only passing.

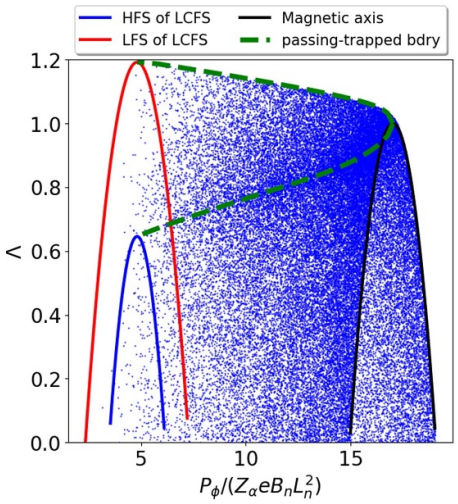

Figure 5. Initial positions of α particle markers (blue points) in the (P_ϕ, Λ) plane. 5×10^4 markers are initially loaded in the simulation. Also shown are the magnetic axis, high-field-side, low-field side of LCFS for α particles of $E = 3.5$ MeV, and the passing trapped boundary (which is independent of the kinetic energy). $B_n = 1$ Tesla, $L_n = 1$ m.

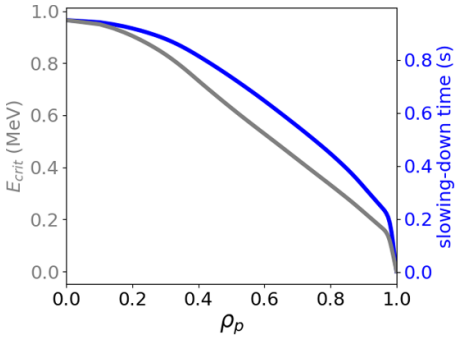

Figure 6. Radial profiles of slowing-down time and critical energy in CFETR hybrid scenario. The formulas calculating the slowing-down time $t^{(s)}$ and critical energy $E_{\rm crit}$ are given equations (B1) and (B3) in the appendix.

Figure 6 plots the radial profiles of the slowing-down time and the critical energy. The slowing-down time is defined as the time span for an α particle of kinetic energy 3.5 MeV to slow down to zero or the cutoff energy $2T_{\rm i}(0)$. Averaging over all the markers in the source gives an average slowing-down time of 0.74 s. (The average slowing-down time observed in the simulation is 0.75 s.) Average value of the critical energy over all the markers is $E_{\rm crit} = 0.65$ MeV.

2.3. Physics model

After sampling the positions and velocity vectors of α particles, the guiding-center positions are calculated. Then the guiding-center drift model is used to follow the particle trajectories in the phase space using the 4th order Runge–Kutta time integration. The average Larmor radius of 3.5 MeV alpha particles initially sampled in the simulations is 1.5% of the machine minor radius. The finite Larmor radius (FLR) effect is taken into account when checking whether a marker touch the first wall. The FLR effect is also included when depositing markers to spatial grids in calculating various moments of the distribution function (e.g. density and pressure). The FLR effect is usually neglected when pushing orbits, to reduce computational cost, i.e. magnetic field values are evaluated at the guiding-centers.

In discussing the α particle co-current flow in section 4, we include the FLR effect when pushing particles. The results show no difference from that of the zero Larmor radius case, indicating gyro-averaged field is not significantly different from the field at the guiding-center.

The collision model for the energetic particles includes the slowing-down, energy diffusion, and pitch angle scattering [14]. The FLR effect is not included when modeling the collisions. We assume a time-independent background plasma. When simulating the continuous birth of α particles and the steady-state (reached when the birth balances the sink (edge

loss + slowing-down)), the results are obtained by doing a single pulse source simulation and integrating in time (making use of the time shift invariance of the problem) to take into account the continuous source.

3. Simulation results

3.1. Time evolution of a pules source

Figure 7 plots the time evolution of particle/power loss fraction and the slowed-down fraction of a pulse α source born at $t=0$. Both the particle and loss fractions are negligibly small (less than 0.3%). The losses are due to first-orbit loss (prompt loss) and collisional loss (neoclassical transport). The results also show that the power loss fraction is lower than the particle loss fraction, as is expected, since α particles are slowed after they are born. Most α particles are slowed down (to the cutoff energy $2T_{\rm i}(0)$) after 1 s. The average slowing-down time observed in the simulation is 0.75 s, which agrees with the analytical estimation given in figure 6.

3.2. Steady-state distribution for continuous source

Figure 8 plots the steady-state distribution in the velocity space for the case of continuous α particle source. To verity that the distribution has reached a steady state at the end of the simulation, figures 8(*b*)–(*d*) plots the distribution at various time slices. The results show that the distribution converges to a steady state.

Figure 8(*d*) shows that the distribution over v_ϕ is not symmetrical about $v_\phi=0$ (the peak slightly shifting to the $v_\phi>0$ region). This implies that the distribution is not isotropic in velocity space. As a result, there is nonzero flow in the direction of $\nabla\phi$ (which is co-current for our case). The distribution over $v_\parallel/v$ also shows similar trend, i.e. there are more co-current particles than counter-current particles. (Co-current corresponds to $v_\parallel/v<0$ because $v_\parallel$ is defined with respect to the magnetic field, which is in the opposite direction of the plasma current in our case.) The net α particle current in this case is 0.3 MA, which is only 2% of the total plasma current (13 MA).

Typical time step size used in the simulations is $\Delta t\Omega_\alpha=2$, where Ω_α is the α particle gyrofrequency at the magnetic axis. To verify the simulations are numerically converged in terms of the time-step size Δt, figure 9 compares f_{v_ϕ} obtained from two simulations using different values of Δt, which shows good agreement, indicating numerical errors are negligible.

If we reverse the poloidal magnetic field direction by the transform $\Psi\to-\Psi$, which will reverse the direction of the plasma current, we found the direction of the residual flow is also reversed, as is shown in figure 10. The flow is always in the co-current direction for positive charged particles. (For negative charged particle, the flow is in the counter-current direction.)

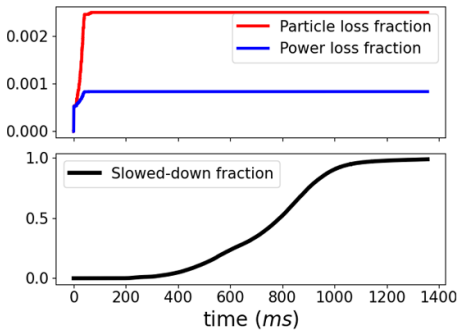

Figure 7. Time evolution of loss fraction and slowed-down fraction of a pulse α source born at $t=0$. The first wall is used as the loss boundary.

Figure 11 compares the steady-state energy distribution obtained in the simulation with the analytical slowing-down and Maxwellian distribution. The slowing-down distribution and Maxwellian distribution are given, respectively, by

$$f_E = C_M\sqrt{E}\exp\left(-\frac{E}{T}\right), \tag{6}$$

and

$$f_E = C_{\rm sd}\frac{\sqrt{E}}{1+\left(\frac{E}{E_{\rm crit}}\right)^{3/2}}, \tag{7}$$

where the normalizing constants, C_M and $C_{\rm sd}$, are decided by the constraint that the two distributions give the same particle number as that in the simulation when integrating over the energy ranges $[0,3.5\,{\rm MeV}]$. The temperature T of the Maxwellian distribution is set to $T=2\overline{E}/3=0.97\,{\rm MeV}$, where $\overline{E}=1.45\,{\rm MeV}$ is the average kinetic energy of α particles observed in the simulation. $E_{\rm crit}$ in equation (7) is set to 0.65 MeV, which is the averaged value among all the markers over the radial profile shown in figure 6.

The results in figure 11 indicate that the simulation result is almost identical to the analytical slowing-down distribution while significantly deviates from the Maxwellian distribution. The results show that Maxwellian distribution underestimates the particle number in the high-energy region ($E>2\,{\rm MeV}$) while overestimates the number in the low-energy region.

Figure 12 plots the steady-state distribution of α particles in (P_ϕ,Λ), (P_ϕ,E), and (E,Λ). One interesting structure is that the peak values of the distribution in (P_ϕ,Λ) plane trace out the passing-trapped boundary. In (E,Λ) plane, we can see that the distribution reach its maximum near $\Lambda=0.9$.

Figure 13 plots the α particle number density in the poloidal plane, where contributions of passing and trapped particles are separated. We found that passing particles density contribution is dominant. Furthermore the results indicate that trapped particles density is not poloidal symmetric, as is expected.

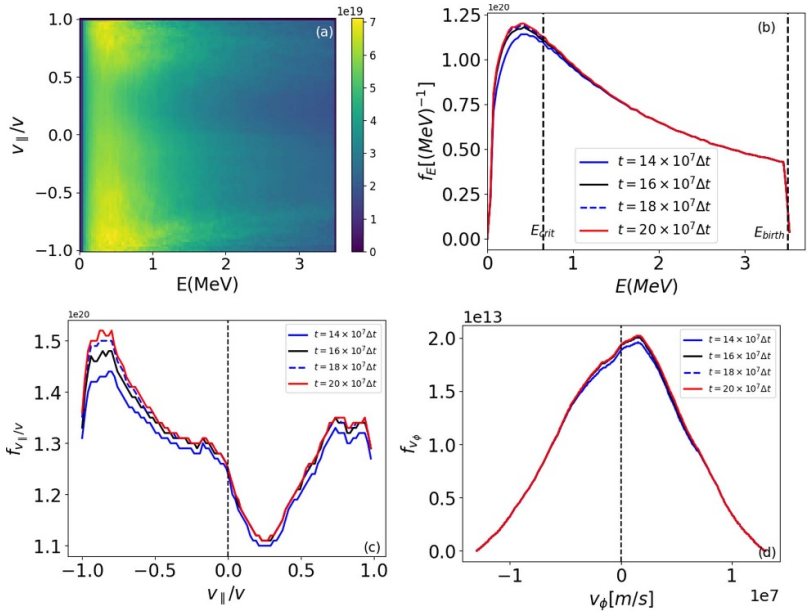

Figure 8. Steady-state distribution of alpha particles in $(E, v_\parallel/v)$ (panel (*a*)), in E (panel (*b*)), in $v_\parallel/v$ (panel (*c*)), and in v_ϕ (panel (*d*)). Here f_E is defined by $f_E \mathrm{d}E = \mathrm{d}N$, where $\mathrm{d}N$ is particle number in energy range $[E, E+\mathrm{d}E]$. And $f_{v_\parallel/v}$ and f_{v_ϕ} are defined in a similar way. Here $E_{\mathrm{crit}} = 0.65\,\mathrm{MeV}$ is the average critical energy.

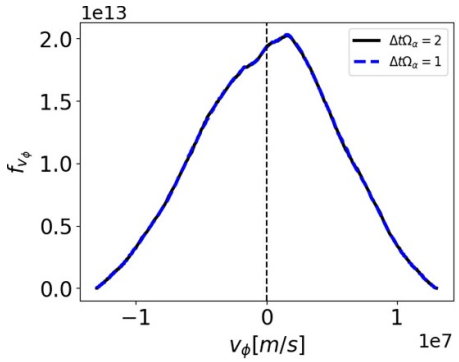

Figure 9. Comparison of f_{v_ϕ} between two simulations using different time step sizes. The black solid line is from figure 8(*d*). The two lines agree with each other very well.

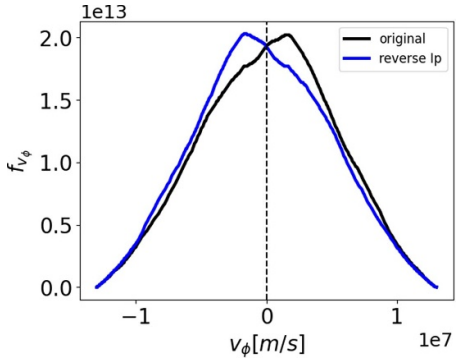

Figure 10. Comparison of f_{v_ϕ} between two cases of opposite plasma currents. The α particle distribution biases to the co-current direction for both the cases, resulting in co-current flow. The black line is from figure 8(*d*).

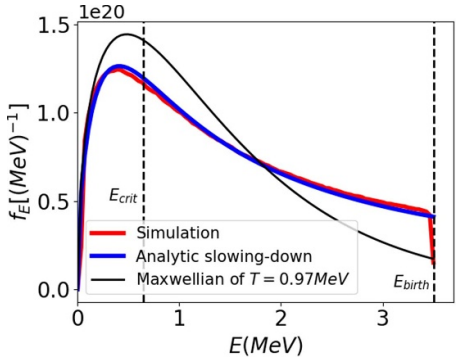

Figure 11. Comparison between simulation, analytical slowing-down, and Maxwellian distribution. The critical energy $E_{\rm crit}$ and birth energy $E_{\rm birth}$ are indicated in the figure.

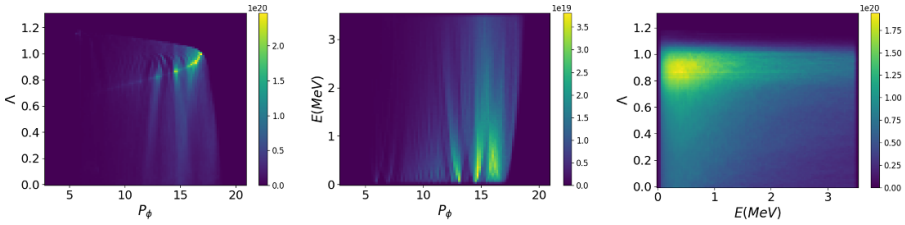

Figure 12. Distribution of α particles in (P_ϕ, Λ), (P_ϕ, E), and (E, Λ), where the unit of P_ϕ is $Z_\alpha e B_n L_n^2$.

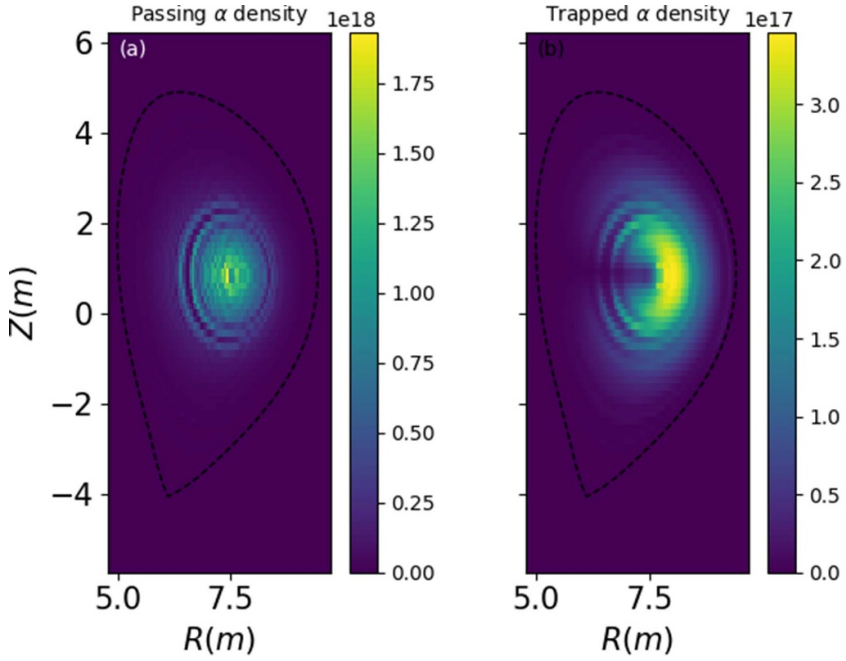

Figure 13. Passing and trapped α particle density in the poloidal plane.

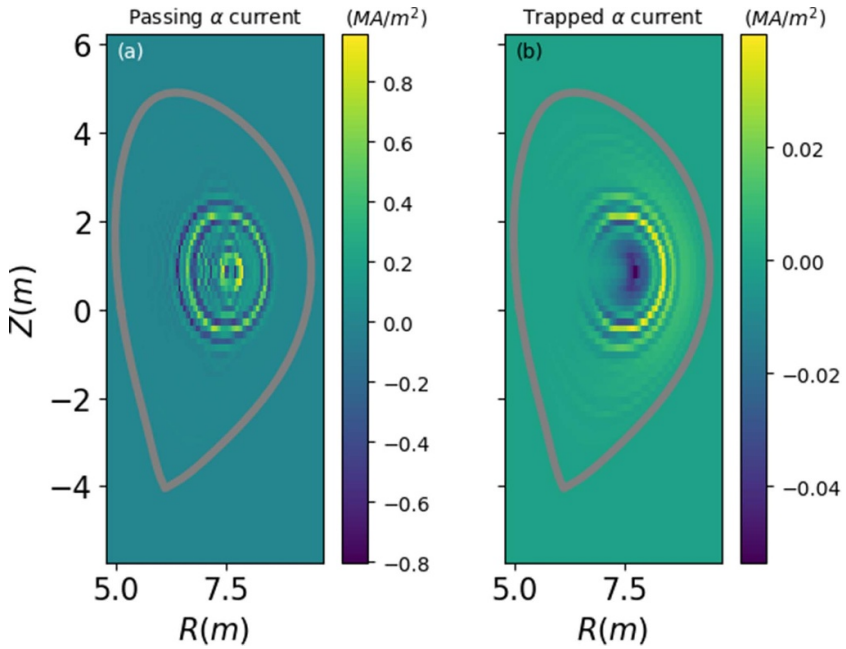

Figure 14. Passing and trapped α particle toroidal current density in the poloidal plane.

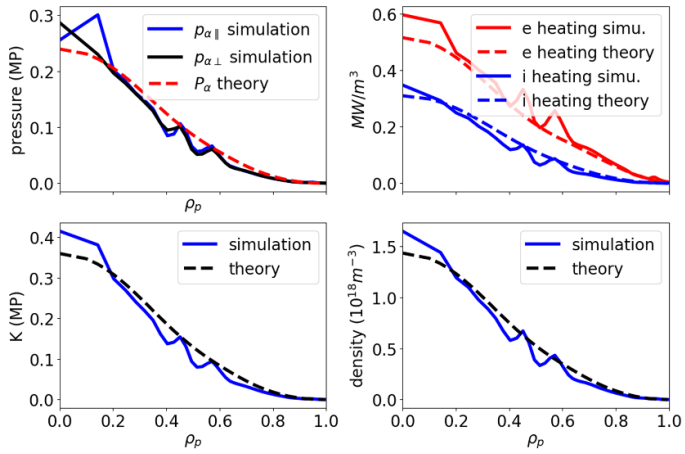

Figure 15. Radial profiles of α particle pressure, heating power density (delivered to electrons and thermal ions), kinetic energy density, and number density. Here the kinetic energy density K is related to $p_{\alpha\parallel}$ and $p_{\alpha\perp}$ by $K = p_{\alpha\parallel}/2 + p_{a\perp}$.

Figure 14 plots the α particle toroidal current density in the poloidal plane, where contributions of passing and trapped particles are also separated. We also found that passing particles' contribution is dominant.

Figure 15 plots the radial profiles of α particle density, pressure, kinetic energy density, and heating power density. Results from analytical theory are also plotted, which are in reasonable agreement with the numerical ones. The results also indicate that $p_{\alpha\parallel}$ and $p_{\alpha\perp}$ are approximately equal to each other, indicating the difference between the parallel and perpendicular dynamics does not generate significant anisotropy in the pressure. Here $p_{\alpha\parallel}$ and $p_{\alpha\perp}$ are defined by

$$p_{\alpha\parallel} = \int m_\alpha v_\parallel^2 f_\alpha \mathrm{d}^3\mathbf{v}, \tag{8}$$

and

$$p_{\alpha\perp} = \int \mu B f_\alpha \mathrm{d}^3\mathbf{v}, \tag{9}$$

respectively, where f_α is the 6D distribution function of α particles. The total pressure is defined by $p_\alpha = (p_{\alpha\parallel} + 2p_{a\perp})/3$. The analytical theory used here is discussed in appendix B.

4. Why anisotropy arises from isotropic source?

4The steady-state α particle distribution is expected to be biased towards co-current direction. This point has been identified in previous works [15–18]. Some authors attributed the anisotropy to asymmetric slowing-down and/or edge loss [18]. The basic reasoning is as follows. More α particles

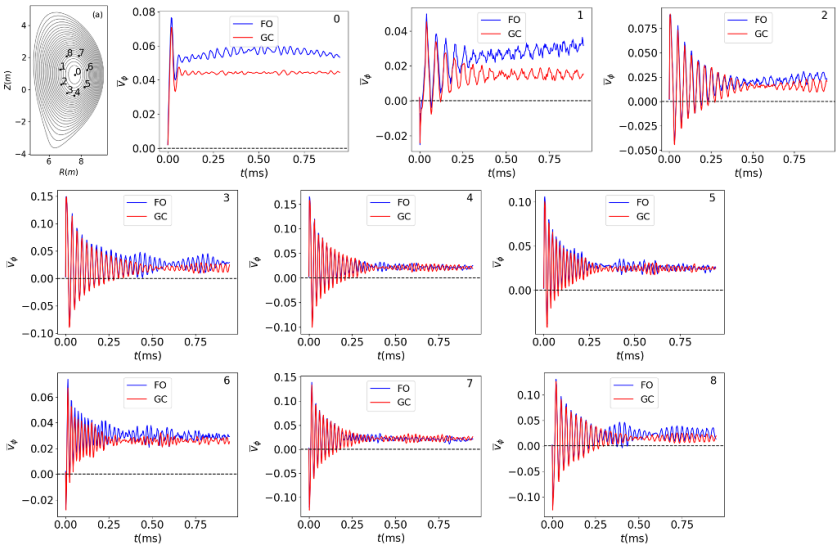

Figure 16. (*a*) Locations of the nine toroidal filament sources in the poloidal plane. (0–8) Time evolution of averaged toroidal velocity, $\overline{v}_\phi$, of each source. The time duration shown is about 100 typical poloidal periods. Unit of $\overline{v}_\phi$ is $7.7\times10^6\,\mathrm{m\,s^{-1}}$. Results from two orbit models are shown: guiding-center (GC) with the FLR effect and full-orbit (FO). The full orbit simulations use the Boris integrator [19] with a time step size $\Delta t\Omega_\alpha = 0.2$, which is 1/10 of that used in the guiding-center simulations.

are born on the low-field side (due to larger volume) than those on the high-field side. So we can focus on the low-field side source. Particles born with co-current velocities on the low-field side have their poloidal orbits more near the core than the corresponding counter-current particles (true for both trapped and passing particles). Therefore co-current particles are less likely to be lost (asymmetric loss) and they also have longer slowing-down time (asymmetric slowing-down) because plasma near the core is hotter. The asymmetric loss and asymmetric slowing-down imply that isotropic source can develop co-current flow.

In fact, the anisotropy can arise even without collisions and edge loss. Here we verify this phenomenon by using direct numerical simulations. We consider a simple collisionless case, where all particles are born at a single time-slice (i.e. pulse source, not continuous source). The source is isotropic in the velocity space with a single energy $E = 3.5\,\mathrm{MeV}$. Furthermore, we limit the source to a single poloidal point and to be toroidally uniform. We follow the Monte–Carlo markers of the source to examine the time evolution of particles' v_ϕ (averaged over all particles, denoted by $\overline{v}_\phi(t)$). The results are shown in figure 16, where 9 sources located at different poloidal locations labeled by 0,1,...8, respectively, are considered.

Figure 16 shows that all the nine sources behavior in similar way. The initial $\overline{v}_\phi$ is near zero (as it should be, since the source is isotropic in velocity space). Later, $\overline{v}_\phi$ deviates from zero and oscillates with time. Then the oscillation amplitude decays with time, which is due to the phase mixing (different particles have different poloidal periods). (At later time, some amplitudes increase a little bit but remain at small values.) An interesting phenomenon is that the time asymptotic trend of $\overline{v}_\phi$ approaches a nonzero positive value (for comparison, the baseline $\overline{v}_\phi = 0$ is indicated in the figure). This corresponds to that particles as a whole are biased to the co-current direction. We will call this co-current flow as residual flow.

To verify that the residual flow is not an artifact of the guiding-center model, we also carried out full orbit simulations of the above case. The results are compared with that of the guiding-center simulations, as is shown in figure 15. The residual flows given by the two models show reasonable agreement (the agreement at location 0 and 1 is not as good as the others). All the residual flows are in the co-current direction.

The residual flow is due to the orbit difference between co-going and counter-going particles. Specifically, co-going particles on average reside in a region of weaker magnetic field than that of the counter-going particles. Figure 17, plots the time evolution of the averaged R of co-going and counter-going particles. The result shows that averaged R of co-going particles is larger than that of the counter-going particles. This means co-going particles on average stay in a region of weaker magnetic field because $B \sim 1/R$. Then as a result of the kinetic energy and magnetic moment conservation, co-going particles will on average have larger parallel velocity than that of counter-going particles. Hence there appears the co-current residual flow.

(Here co- and counter-going refer to a specific time slice ($t = 0$). For trapped particles, their v_ϕ will change sign later, but they are still classified into co-going or counter-going according to their initial v_ϕ signs. If we consider only trapped particles, the difference of $\overline{R}$ between co-going and counter-going is not significant, and the trend can be reversed (not shown). Because particle number of the passing particles is dominant in these cases, the overall trend is determined by the passing particles.)

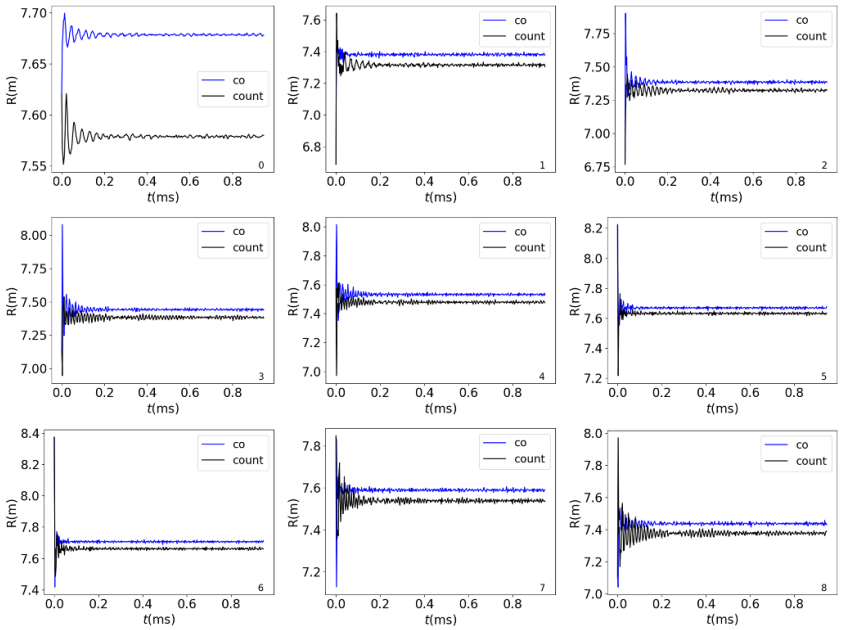

Figure 17. Time evolution of averaged R of a pulse source at the 9 poloidal points indicated in figure 16.

This residual flow is a universal mechanism for spontaneous co-current rotation in tokamaks, i.e, a positively charged source of zero momentum turns out to rotate in the co-current direction. This is related to the bootstrap effect that gives rise to the bootstrap current, but is of less importance for thermal particles because their orbit deviation from magnetic surfaces is much smaller than that of energetic particles.

We note that the momentum of the system should be conserved. What is the origin of the net momentum in the residual flow? In the simple case of collisionless simulations, the sole contributor is the magnetic field. I.e., the momentum is derived from the magnetic coils of the facility.

5. Effects of ripple field

The effects of the ripple field on α particles loss in CFETR have been studied in previous works [20–22]. Improvements over these works are possible, e.g. using the first wall instead of the LCFS as the loss boundary, including all the three components of the ripple field rather than only the toroidal component, and making sure that the curl-free condition is respected. The ripple field used in this work is discussed in appendix C. For the hybrid scenario studied in this work, we found the ripple loss is small: power loss fraction is less than 0.2%, as is shown in figure 18.

We found the effect of the ripple field on the α particle steady-state distribution is also small, with the difference nearly invisible to eyes when compared. An example is shown in figure 19, which compares the f_{v_ϕ} between the case without ripple and that with ripple.

The ripple field, as a kind of 3D perturbation to the 2D equilibrium field, usually has a damping effect on plasma flow via the so-called neoclassical viscosity torque. The results in figure 19 indicate that this damping effect happens to be small for this specific case. Also we note that the ripple field mainly influences trapped particles (region near $v_\phi = 0$ in figure 19) while the residual flow of α particles mainly comes

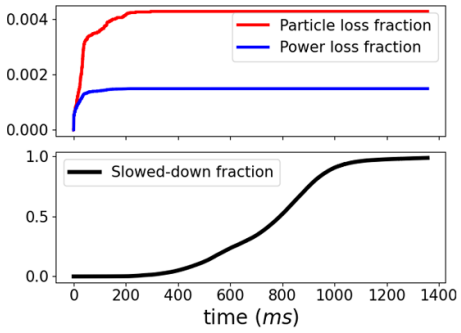

Figure 18. The same as figure 7 except that this is with ripple field. The power loss fraction is about twice of that of the case without ripple field.

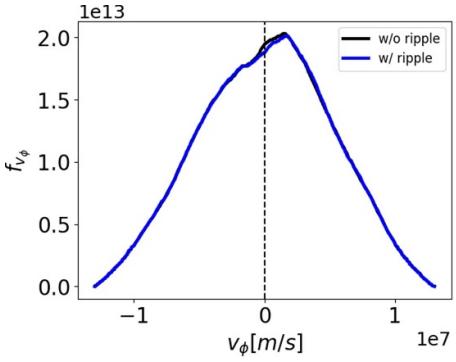

Figure 19. Comparison of f_{v_ϕ} between the case without ripple and that with ripple.

from passing particles. This implies the ripple field effect on the residual flow should be weak.

6. Summary and discussion

We carried out systematic study of neoclassical equilibrium distribution of α particles born from DT nuclear fusion in a tokamak reactor. Simulation results of α particle radial profiles are in reasonable agree with analytical theory. This provides a verification for the simulation code. The agreement also indicates that the finite drift orbit width and other effects that are included in the simulation are not important in determining these profiles (density, pressure, heating power density). We also found that the ripple field has negligible effects on the steady-state distribution in the hybrid scenario considered in this paper.

In the process of this study, we identified a previously known but less investigated phenomenon—the co-current flow of α particles. This weak flow can be reliably observed in simulations. This also provide confidence in the numerical accuracy of the simulations. Previous works on the anisotropy (the flow) suggest that collisions or/and edge loss are needed in forming the anisotropy. Our finding is that even in the case without collisions and edge loss, the anisotropy can still appear. We gave a clear demonstration of the process by simple numerical simulations: the collisionless evolution of toroidal filament sources. We found that the flow appears because of the co-count asymmetry, which make co-going α particles on average stay in a weaker field side than that of the counter-going ones.

The net α particle current in our specific case is 0.3 MA, which is only 2% of the total plasma current (13 MA). Whether this fraction can be significantly increased by optimizing the plasma scenarios is not clear. As a future research option, we may study how the aspect ratio and plasma shape influence this fraction.

Data availability statement

The data that support the findings of this study are available upon reasonable request from the corresponding author.

Acknowledgment

Y. Hu thanks Deng Zhou and Lei Ye for useful discussions. Numerical computations in this work were performed on Sugon ChaohuMingYue computing center in Hefei. This work was supported by the Strategic Priority Research Program of Chinese Academy of Sciences under Grant No. XDB0790203, and by the National Natural Science Foundation of China under Grant No. 12475234.

Conflict of interest

The authors have no conflicts to disclose.

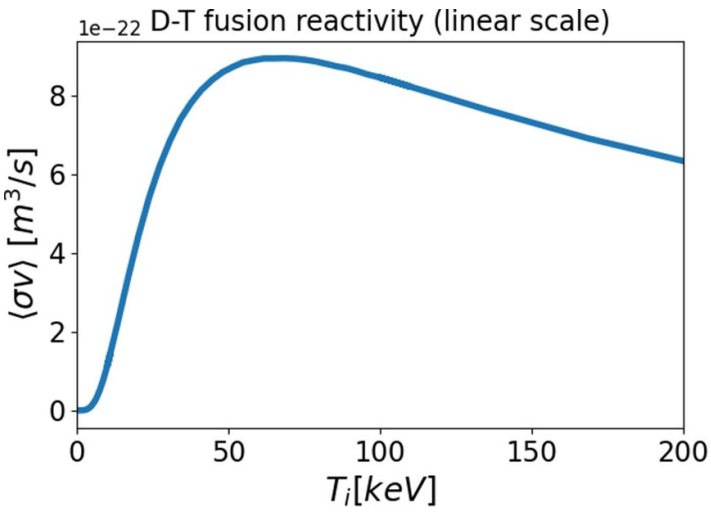

Figure 20. The deuterium–tritium reactivity $\langle\sigma v\rangle$ vs. temperature for Maxwellian distribution of the same temperature. Peak fusion reactivity occurs at $T_i = 68.6\,\mathrm{keV}$. Mote–Carlo sampling and integration are used in performing the 6D phase-space integration in equation (A2).

Appendix A. Fusion rate

The fusion rate F_{rate} is defined by

$$F_{\mathrm{rate}} = n_1 n_2 \langle\sigma v\rangle, \tag{A1}$$

with the reactivity

$$\langle\sigma v\rangle \equiv \frac{1}{n_1 n_2}\int \sigma|\mathbf{v}_1 - \mathbf{v}_2| f_1(\mathbf{v}_1) f_2(\mathbf{v}_2)\,\mathrm{d}\mathbf{v}_1\mathrm{d}\mathbf{v}_2, \tag{A2}$$

where n_1 and n_2 are number densities of the reactants. A frequently used fitting formula for fusion cross section σ is given by Bosch and Hale [23]. Using that formula and assuming Maxwellian distribution of the same temperature for reactants, we calculated the deuterium–tritium reactivity $\langle\sigma v\rangle$ as a function of the temperature, which is plotted in figure 20. This is the case used in this paper. Other reactions such as beam-thermal reactions are not included.

Appendix B. Theory of α particle steady-state distribution and heating power density

Assume α particles stay on the same magnetic surfaces where they are born (zero orbit-width approximation), then the time for a particle of kinetic energy E_{birth} to slow down to zero can be analytically obtained [24]:

$$t_{\mathrm{s}} = \frac{t_{\mathrm{se}}}{3}\ln\left[1 + \left(\frac{E_{\mathrm{birth}}}{E_{\mathrm{crit}}}\right)^{3/2}\right] \tag{B1}$$

where

$$t_{\mathrm{se}} = \frac{3(2\pi)^{3/2} T_{\mathrm{e}}^{3/2}\epsilon_0^2}{n_{\mathrm{e}} Z_\alpha^2 e^4 \ln\Lambda^{\alpha/e}}\frac{m_\alpha}{\sqrt{m_{\mathrm{e}}}}, \tag{B2}$$

$$E_{\mathrm{crit}} = T_{\mathrm{e}}\left(\frac{3\sqrt{\pi}}{4}\sum_i \frac{m_{\mathrm{e}} n_i Z_i^2}{m_i n_{\mathrm{e}}}\right)^{2/3}, \tag{B3}$$

where $Z_i = q_i/e$ is the charge number of bulk ion species i. (Note that, due to the ion mass dependence, the sum over the bulk ion species can not be written in terms of $Z_{\mathrm{eff}} \equiv \sum_i n_i Z_i^2/n_{\mathrm{e}}$.)

B.1. Steady-state energetic α particle density and pressure

The steady-state density of energetic α particles at a radial location is then given by

$$\begin{aligned} n_\alpha(\psi) &= \int_0^{t_s} F_{\text{rate}}(\psi)\,\mathrm{d}t \\ &= F_{\text{rate}}(\psi)\,\frac{t_{\text{se}}}{3}\ln\left[1+\left(\frac{E_{\text{birth}}}{E_{\text{crit}}}\right)^{3/2}\right]. \end{aligned} \tag{B4}$$

where $F_{\text{rate}} = n_{\text{D}} n_{\text{T}} \langle \sigma v \rangle$ is the fusion rate $(\mathrm{m}^{-3}\mathrm{s}^{-1})$.

Similarly, the steady-state kinetic energy density K_α at a radial location is given by

$$K_\alpha = \int_0^{t_s} E(t)\,F_{\text{rate}}\mathrm{d}t = F_{\text{rate}}\int_0^{t_s} E(t)\,\mathrm{d}t, \tag{B5}$$

where $E(t)$ is the instantaneous kinetic energy of an α particle, Using $E(t)$ given by equation (5.4.11) in Wesson's book [24], the above integration can be analytically performed, giving

$$\begin{aligned} K_\alpha = F_{\text{rate}} E_{\text{birth}} t_{\text{se}} \Bigg[&-\frac{1}{6y}\ln\left(\frac{\left|y-\sqrt{y}+1\right|}{\left(\sqrt{y}+1\right)^2}\right) \\ &-\frac{\arctan\left(\frac{2\sqrt{y}-1}{\sqrt{3}}\right)}{\sqrt{3}y} - \frac{\arctan\left(1/\sqrt{3}\right)}{\sqrt{3}y} + \frac{1}{2}\Bigg], \end{aligned} \tag{B6}$$

where $y = E_{\text{birth}}/E_{\text{crit}}$. Note that F_{rate}, t_{se} and E_{crit} (and thus y) depend on the radial position. Equation (B6) agrees with equation (5.B-9) in the technical report of the plasma transport code ONETWO [25].

The α particle pressure is related to K_α by $P_\alpha = 2K_\alpha/3$.

B.2. Steady-state heating power density (delivered to ions and electrons) from energetic α particles

The steady-state heating power density (delivered to background plasma) from α particles is given by

$$\begin{aligned} H &= \int_0^{t_s}\left(-\frac{\mathrm{d}E}{\mathrm{d}t}\right)F_{\text{rate}}(\psi)\,\mathrm{d}t. \\ &= -F_{\text{rate}}(\psi)\int_0^{t_s}\mathrm{d}E \\ &= F_{\text{rate}}(\psi)\,E_{\text{birth}}. \end{aligned} \tag{B7}$$

The slowing-down dynamics can be split into two parts (electron/ion contribution):

$$\left(\frac{\mathrm{d}E}{\mathrm{d}t}\right)_{\text{e}} = -\frac{2}{t_{\text{se}}}E \tag{B8}$$

and

$$\left(\frac{\mathrm{d}E}{\mathrm{d}t}\right)_{i} = -\frac{2}{t_{\text{se}}}E\left(\frac{E_{\text{crit}}}{E}\right)^{3/2} \tag{B9}$$

Then, the steady-state heating power density delivered to background electrons is written as

$$\begin{aligned} H_{\text{e}} &= \int_0^{t_s}\left[-\left(\frac{\mathrm{d}E}{\mathrm{d}t}\right)_{e}\right]F_{\text{rate}}(\psi)\,\mathrm{d}t. \\ &= F_{\text{rate}}(\psi)\,\frac{2}{t_{\text{se}}}\int_0^{t_s} E\mathrm{d}t \end{aligned} \tag{B10}$$

$$= K_\alpha\frac{2}{t_{\text{se}}}. \tag{B11}$$

Similarly, the steady-state heating power density delivered to background ions is written as

$$\begin{aligned} H_i &= \int_0^{t_s} \left[-\left(\frac{\mathrm{d}E}{\mathrm{d}t}\right)_i \right] F_{\mathrm{rate}}(\psi)\,\mathrm{d}t. \\ &= F_{\mathrm{rate}}(\psi)\,\frac{2}{t_{\mathrm{se}}} E_{\mathrm{crit}}^{3/2} \int_0^{t_s} \frac{1}{\sqrt{E}}\mathrm{d}t, \end{aligned} \tag{B12}$$

Here we note that the integrand is singular at $E(t=t_s)=0$. To avoid this difficulty, we can choose a cutoff energy which is not exactly zero. We can also calculate H_i by $H_i = H - H_e$, which avoids direct calculation of the above integration.

Appendix C. Ripple field

Some works on ripple loss retain only the toroidal component of ripple field, neglecting the poloidal component [22]. In this work, we retain all the three components and take into account the constraints of curl-free and divergence-free. Assume that the ripple filed $\tilde{\mathbf{B}}$ is determined solely by currents outside the plasma [26], then $\tilde{\mathbf{B}}$ in the plasma satisfies the curl-free and divergence-free conditions, i.e.

$$\nabla \cdot \tilde{\mathbf{B}} = 0 \tag{C1}$$

$$\nabla \times \tilde{\mathbf{B}} = 0 \tag{C2}$$

In the cylindrical coordinates, equation (C1) is written as

$$\frac{1}{R}\frac{\partial}{\partial R}\left(R\tilde{B}_R\right) + \frac{1}{R}\frac{\partial \tilde{B}_\phi}{\partial \phi} + \frac{\partial \tilde{B}_Z}{\partial Z} = 0, \tag{C3}$$

and the R, ϕ, and Z components of equation (C2) are written as

$$\frac{1}{R}\frac{\partial \tilde{B}_Z}{\partial \phi} - \frac{\partial \tilde{B}_\phi}{\partial Z} = 0, \tag{C4}$$

$$\frac{\partial \tilde{B}_R}{\partial Z} - \frac{\partial \tilde{B}_Z}{\partial R} = 0, \tag{C5}$$

$$\frac{1}{R}\frac{\partial}{\partial R}\left(R\tilde{B}_\phi\right) - \frac{1}{R}\frac{\partial \tilde{B}_R}{\partial \phi} = 0. \tag{C6}$$

Assume that the toroidal component of the ripple field can be well represented by a single toroidal harmonic, $n=N$, where N is the number of toroidal field (TF) coils. Suppose that the toroidal locations of TF coil centers are $\phi = 2\pi j/N$ with $j = 0,1,\ldots,N-1$. Then, without loss of generality, we write $\widetilde{B_\phi}$ as

$$\tilde{B}_\phi = B_{\phi 0}(R,Z) f(R,Z) \cos(N\phi), \tag{C7}$$

where $f(R,Z)$ is a unknown function of non-negative value, $B_{\phi 0}$ is the $n=0$ harmonic of the toroidal component of the magnetic field generated by the TF coils.

(We note that f introduced above is just the ripple amplitude of the toroidal field, $\delta(R,Z)$, which is defined by

$$\delta(R,Z) = \mathrm{sign}(B_{\phi 0}) \frac{B_\phi^{(\max)} - B_\phi^{(\min)}}{B_\phi^{(\max)} + B_\phi^{(\min)}}, \tag{C8}$$

where the superscript 'max' means taking maximum along the ϕ direction. Using $B_\phi = B_{\phi 0}(R,Z) + \tilde{B}_\phi(R,Z,\phi)$, the above expression is written as

$$\delta(R,Z) = \frac{2B_{\phi 0} f}{2B_{\phi 0}} = f, \tag{C9}$$

i.e. f is identical to δ.)

Substituting expression (C7) into equation (C3), we know that the dependence of $\tilde{B}_R$ and $\tilde{B}_Z$ on ϕ must be $\sin(N\phi)$, i.e. $\tilde{B}_R$ and $\tilde{B}_Z$ have $\pi/2$ toroidal phase difference from that of $\tilde{B}_\phi$. Then, without loss of generality, $\tilde{B}_R$ and $\tilde{B}_Z$ can be written as

$$\tilde{B}_R = B_{\phi 0} g(R,Z) \sin(N\phi), \tag{C10}$$

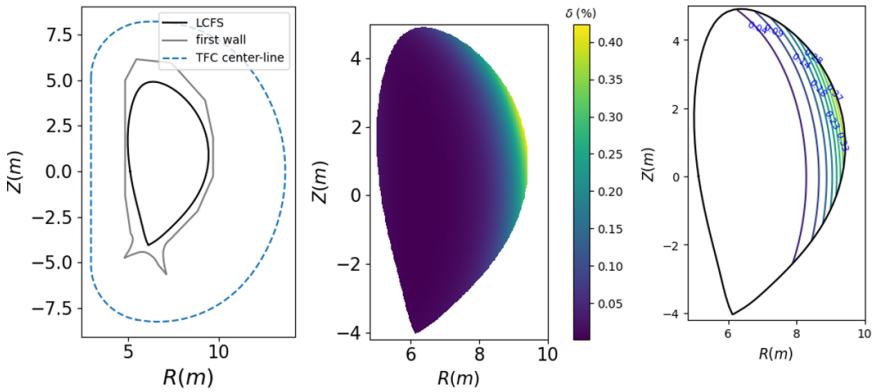

Figure 21. Left: TF coil central line, first wall, and LCFS. There are 16 TF coils ($N = 16$). Each coil has 154 turns with nominal current 95.6 kA/turn. Middle: Color map of ripple degree δ within the LCFS. Right: Contours of the ripple.

$$\tilde{B}_Z = B_{\phi 0} h\left(R,Z\right) \sin\left(N\phi\right), \tag{C11}$$

where g and h are unknown functions to be determined, which can be determined by the curl-free constraint, as follows. Using the expressions of B_Z and B_ϕ in equation (C4), we obtain

$$h = \frac{R}{NB_{\phi 0}} \frac{\partial B_{\phi 0} f}{\partial Z}. \tag{C12}$$

Similarly, using the expressions of $\tilde{B}_R$ and $\tilde{B}_\phi$ in equation (C6), we obtain

$$g = \frac{1}{NB_{\phi 0}} \frac{\partial}{\partial R} \left(R B_{\phi 0} f\right) \tag{C13}$$

(We note that the last equation of the curl-free condition, equation (C5), is automatically satisfied when h and g takes the forms given by equations (C12) and (C13). Therefore, all the component equations of the curl-free condition are satisfied.) Using the above results, the divergence-free condition is finally written as

$$\frac{\partial}{\partial R}\left(R \frac{\partial}{\partial R}\left(R B_{\phi 0} f\right)\right) - B_{\phi 0} f N^2 + R^2 \frac{\partial^2}{\partial Z^2}\left(B_{\phi 0} f\right) = 0. \tag{C14}$$

How well this constraint is satisfied depends on the accuracy of $\tilde{B}_\phi$ amplitude, i.e. $B_{\phi 0} f$, which is numerically obtained. In this work, B_ϕ generated by the 16 TF coils is computed by integrating the TF coil currents using the Biot–Savart law. We use filament currents along the TF coil center-lines to approximate the currents in the TF coils. Values of B_ϕ in two poloidal planes ($\phi = 0$ and $\phi = \pi/N$) are computed. Then $f B_{\phi 0}$ is computed by

$$f B_{\phi 0} = \frac{B_\phi\left(R,Z,\phi = 0\right) - B_\phi\left(R,Z,\phi = \pi/N\right)}{2}. \tag{C15}$$

Figure 21 plots the TF coil central line and ripple degree of CFETR.

Figure 22 plots the amplitudes of $\tilde{B}_R$, $\tilde{B}_Z$, and $\tilde{B}_\phi$, which shows that the amplitudes of $\tilde{B}_R$ and $\tilde{B}_\phi$ are of similar magnitude, indicating the necessity of taking into account the poloidal components.

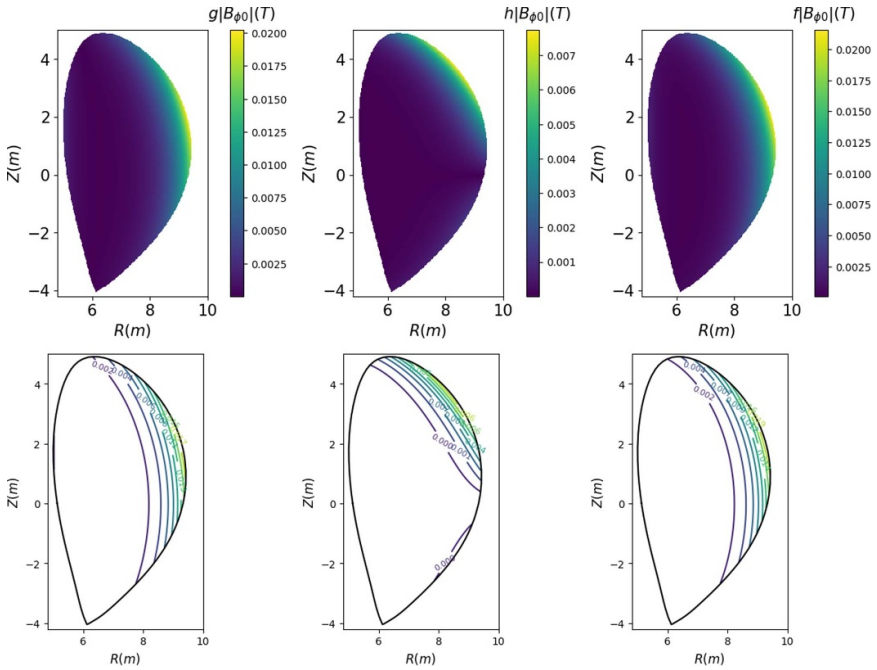

Figure 22. The amplitudes of $\tilde{B}_R$ (left), $\tilde{B}_Z$ (middle), $\tilde{B}_\phi$ (right). The low panel is the corresponding contours.

ORCID iDs

Xingyuan Xu https://orcid.org/0000-0001-6674-1811
Yingfeng Xu https://orcid.org/0000-0003-2960-9488
Yifeng Zheng https://orcid.org/0000-0003-0630-5289
Guoqiang Li https://orcid.org/0000-0003-0792-4348
Zhiyong Qiu https://orcid.org/0000-0002-7548-8819
Youwen Sun https://orcid.org/0000-0002-9934-1328

References

[1] Chen J., Chan V.S., Jian X., Zhang X., Ren Q., Li G. and Zhou C. (CFETR Physics Team) 2021 *Nucl. Fusion* **61** 046002
[2] Hu Y., Xu X., Hu Y., He K. and Wang J. 2023 *Phys. Plasmas* **30** 092507
[3] Pankin A., Mccune D., Andre R., Bateman G. and Kritz A. 2004 *Comput. Phys. Commun.* **159** 157
[4] Tani K., Azumi M., Kishimoto H. and Tamura S. 1981 *J. Phys. Soc. Japan* **50** 1726
[5] Hirvijoki E., Asunta O., Koskela T., Kurki-Suonio T., Miettunen J., Sipilä S., Snicker A. and Äkäslompolo S. 2014 *Comput. Phys. Commun.* **185** 1310
[6] White R.B., Gorelenkov N., Heidbrink W.W. and Zeeland M.A.V. 2010 *Plasma Phys. Control. Fusion* **52** 045012
[7] Kramer G.J., Budny R.V., Bortolon A., Fredrickson E.D., Fu G.Y., Heidbrink W.W., Nazikian R., Valeo E. and Van Zeeland M.A. 2013 *Plasma Phys. Control. Fusion* **55** 025013
[8] Pfefferlé D., Cooper W., Graves J. and Misev C. 2014 *Comput. Phys. Commun.* **185** 3127
[9] Xu Y., Guo W., Hu Y., Ye L., Xiao X. and Wang S. 2019 *Comput. Phys. Commun.* **244** 40
[10] He K., Sun Y., Wan B.N., Gu S., Jia M. and Hu Y. 2020 *Nucl. Fusion* **61** 016009
[11] Wang F., Zhao R., Wang Z.-X., Zhang Y., Lin Z.-H. and Liu S.-J. 2021 *Chin. Phys. Lett.* **38** 055201
[12] Ye L., Guo W., Xiao X., Dai Z. and Wang S. 2014 *Phys. Plasmas* **21** 122508
[13] Lao L., John H.S., Stambaugh R., Kellman A. and Pfeiffer W. 1985 *Nucl. Fusion* **25** 1611
[14] Todo Y., Zeeland M.V., Bierwage A. and Heidbrink W. 2014 *Nucl. Fusion* **54** 104012
[15] Schneider M., Eriksson L.-G., Basiuk V. and Imbeaux F. 2005 *Plasma Phys. Control. Fusion* **47** 2087
[16] Honda M., Takizuka T., Tobita K., Matsunaga G. and Fukuyama A. 2011 *Nucl. Fusion* **51** 073018
[17] Snicker A., Asunta O., Ylitie H., Kurki-Suonio T., Schneider M. and Pinches S.D. 2015 *Nucl. Fusion* **55** 063023
[18] Salewski M. *et al* 2018 *Nucl. Fusion* **58** 096019
[19] Hu Y., Miecnikowski M.T., Chen Y. and Parker S.E. 2018 *Plasma* **1** 105
[20] Zhao R., Wang Z.-X., Wang F. and Hao B.-L. 2020 *Plasma Phys. Control. Fusion* **62** 115001
[21] Hao B. *et al* 2021 *Nucl. Fusion* **61** 046035
[22] Xu Y., Zhang D., Chen J. and Zhong F. 2022 *Plasma Sci. Technol* **24** 105101
[23] Bosch H.-S. and Hale G. 1992 *Nucl. Fusion* **32** 611
[24] Wesson J. 2004 *Tokamaks* (Oxford University Press)
[25] Pfeiffer W.W., Davidson R.H., Miller R.L., and Waltz R.E. 1980 Onetwo: a computer code for modeling plasma transport in tokamaks *Technical Report* General Atomics
[26] Mcclements K.G. 2005 *Phys. Plasmas* **12** 072510